HHS Public Access

Author manuscript

Bioconjug Chem. Author manuscript; available in PMC 2019 February 19.

Published in final edited form as:

Bioconjug Chem. 2018 September 19; 29(9): 2982–2993. doi:10.1021/acs.bioconjchem.8b00400.

Zero-Dimensional Carbon Dots Enhance Bone Regeneration, Osteosarcoma Ablation, and Clinical Bacterial Eradication

Yao Lu[†,‡], **Lihua Li**[‡,§], **Mei Li**[‡], **Zefeng Lin**[‡], **Liping Wang**[§], **Yu Zhang**[‡], **Qingshui Yin**[*,‡], **Hong Xia**[*,‡], and **Gang Han**[*,⊥]

[†]Department of Orthopedics, Zhujiang Hospital, Southern Medical University, 253 Gongye Road, Guangzhou, Guangdong 510282, China

[‡]Guangdong Key Laboratory of Orthopedic Technology and Implant Materials, Key Laboratory of Trauma and Tissue Repair of Tropical Area of PLA, Department of Orthopedics, Guangzhou General Hospital of Guangzhou Military Command of PLA, 111 Liuhua Road, Yuexiu District, Guangzhou, Guangdong 510010, China

[§]China-Germany Research Center for Photonic Materials and Device the State Key Laboratory of Luminescent Materials and Devices, Guangdong Provincial Key Laboratory of Fiber Laser Materials and Applied Techniques School of Materials Science and Engineering, South China University of Technology, 381 Wushan Road, Guangzhou, Guangdong 510641, China

[⊥]Department of Biochemistry and Molecular Pharmacology, University of Massachusetts Medical School, Worcester, Massachusetts 01605, United States

Abstract

Zero-dimensional carbon dots (CD) and their effects on osteogenesis have been rarely studied in bone repair scaffolds. Here, we fabricate a novel CD doped chitosan/nanohydroxyapatite (CS/nHA/CD) scaffold with full potential to promote bone regeneration by a facile freeze-drying method. The CS/nHA/CD scaffolds enhanced cell adhesion and osteoinductivity in rat bone mesenchymal stem cells by up-regulating genes involved in focal adhesion and osteo-genesis *in vitro*, which significantly improved the formation of vascularized new bone tissue at 4 weeks compared to pure CS/nHA scaffolds *in vivo*. Inspired by the excellent photo-thermal effect of CD, the scaffolds were applied in tumor photothermal therapy (PTT) under near-infrared (NIR) irradiation (808 nm, 1 W/cm^2). The scaffolds significantly inhibited osteosarcoma cell proliferation *in vitro* and effectively suppressed tumor growth *in vivo*. Moreover, the CS/nHA/CD scaffolds possessed distinct antibacterial properties toward clinically collected *S. aureus* and *E. coli*, and their antibacterial activity was further enhanced under NIR irradiation. This work demonstrates that zero-dimensional CD can enhance the osteogenesis-inducing property of bone

[*]**Corresponding Authors:** gz_yqs@126.com (Q.-S.Y.). gzxiahong2@126.com (H.X.). gang.han@umassmed.edu (G.H.).

Supporting Information

The Supporting Information is available free of charge on the ACS Publications website at DOI: 10.1021/acs.bioconjchem.8b00400. Experimental section; morphology and zeta potential of CD; SEM analysis of the scaffolds; effect of ionic strength on scaffold integrity; photothermal effects of CD *in vitro*; photothermal effect of the scaffolds *in vitro*; cytotoxity of the scaffolds; hemolysis tests of the scaffolds; H&E staining of the main organs; antibacterial effect of the scaffolds *in vitro* (PDF)

The authors declare no competing financial interest.

repair scaffolds and that CD doped scaffolds have potential for use in PTT for tumors and infections.

Graphical Abstract

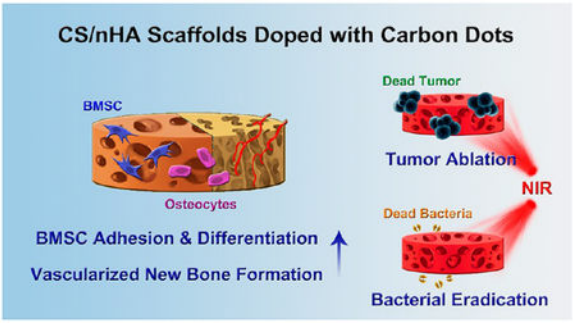

INTRODUCTION

Bone defects and their repair are one of the most common global health issues. Current therapies include autografts, allografts, and xenografts, but limitations, such as donor shortage, pathogen transfer, and immune response, still exist.[1] In recent years, biocompatible three-dimensional scaffolds for bone tissue engineering have attracted considerable attention,[2,3] and various materials, such as metals,[4] ceramics,[5] and polymers,[6] have been explored to synthesize scaffolds to fill the missing bone. Bone is a natural organic−inorganic biocomposite mainly composed of collagen and nanohydroxyapatite (nHA, $Ca_{10}(PO_4)_6(OH)_2$). Organic−inorganic composite scaffolds have been developed to mimic bone constituents and structures. Chitosan (CS) is a natural polysaccharide with numerous advantages, such as biocompatibility, biodegradability, and low immunogenicity.[7,8] Unlike collagen, the CS has a rigid crystalline structure that promotes mesenchymal stem cells to differentiate into osteoblasts.[9,10] Moreover, CS has notable biofunctions, including antimicrobial, antifungal, and antioxidant activities.[11–13] nHA constitutes 50–70% of human bone and is also histocompatible and osteoinductive.[14] Hence, CS and nHA composites are appropriate candidates for basic bone repair scaffolds.

One approach to enhancing the osteogenic performance of the scaffolds is to use growth factors and chemical reagents in the scaffolds, such as bone morphogenetic proteins, vesicular endothelial growth factors, and dexamethasone.[15,16] Recently, carbon-based nanomaterials, such as single-walled carbon nanotubes (SWNT), multiwalled carbon nanotubes (MWNT), and graphene/graphene oxide (GO), have demonstrated efficacy in tissue engineering, especially with regard to the ability of their specific surface properties to guide mesenchymal stem cell osteogenesis.[17,18] Zero-dimensional carbon dots (CD) are cost-effective carbon-based nanomaterials that can be cheaply produced by various methods.[19] For example, microwave synthesis is a popular method because its low cost and ability to be simply achieved in a few minutes.[20] In addition, CD also show apparent advantages for bioapplications, namely, low cytotoxicity and water solubility.[21,22]

Very recently, CD synthesized from carbon nanopowder were reported to specifically bind to calcified bones *in vivo*.[23] Citric acid–base CD are also found to track and enhance differentiation of rat bone mesenchymal stem cells (rBMSCs).[24] Erdal et al.[25] have prepared nanographene oxide (r-nGO) CD incorporated poly(*ε*-caprolactone) (PCL) films with better formation of hydroxyapatite minerals on the surface. Khajuria et al.[26] have reported nitrogen doped CD/hydroxyapatite (NCDs-HA) can promote osteoblast cells (MC3T3-E1) osteogenic differentiation and bone regeneration in a zebrafish model. However, CD have been rarely used in the three-dimensional bone scaffolds, and their influence on the stem cell behavior and *in vivo* osteoinductivity has not been well studied. In addition, bone defects can be caused by various etiologies, such as trauma, tumor resection, and infections. CD can exhibit photothermal effects under near-infrared (NIR) irradiation,[27] giving CD doped scaffolds potential in photo-thermal therapy (PTT) for tumors and infections in bone and then filling and repairing bone defects simultaneously.

Herein, we report a novel CS/nHA/CD scaffold prepared by facile physical mixing and lyophilization. In a series of *in vitro* and *in vivo* studies, the as-synthesized scaffolds showed a porous structure favoring rat bone mesenchymal stem cells (rBMSCs) adhesion by promoting gene expression of the focal adhesion pathway. Furthermore, the CS/nHA/CD scaffold enhanced *in vitro* osteogenesis of rBMSCs by up-regulating their expression of osteogenic genes and significantly facilitated the formation of vascularized new bone tissue *in vivo* compared to the pure CS/nHA scaffold. The scaffold exhibited outstanding photothermal effects under NIR laser irradiation and effectively induced tumor cell death *in vitro* due to the doping of CD. After implanting the scaffold into an osteosarcoma-bearing mouse model, the highly malignant tumor was significantly inhibited *in vivo* under NIR irradiation. Moreover, their antibacterial properties toward clinical pathogenic bacteria can be significantly strengthened both *in vitro* and *in vivo* after NIR irradiation. Consequently, CS/nHA/CD scaffolds with enhanced osteogenesis-inducing ability can be used to fill bone defects, ablate tumors, and kill clinically derived bacteria.

RESULTS AND DISCUSSION

Fabricating and Characterization of the Scaffolds.

CD were synthesized by a classic microwave method,[20] and the size was about 5 nm (Figure S1, Supporting Information). Figure 1a and Figure S2 show the morphology of the prepared scaffolds. All scaffolds had porous and highly interconnected structures with similar pore sizes (ranging from 30 to 70 μm). CD could be found in the TEM image of the CS/nHA/CD scaffolds (Figure 1b). The FTIR spectra of CD, CS/nHA, and CS/nHA/CD were also investigated. In the spectra of CD, the broad absorption bands at 3368–3564 cm^{-1} were assigned to OH/NH_2 vibration, which ensure their hydrophilic and stability. Absorption at 1547 and 1706 cm^{-1} were assigned to the vibration of C=O. The zeta potential of CD is −74.7 mV (Figure S1, Supporting Information), owning to the abundant negative OH and COO- on the CD surface. After doping the negative CD into the cationic CS polymer, the corresponding vibration peaks of CS/nHA/CD scaffolds exhibit enhancement and redshift compared to the CS/nHA scaffolds. These results indicate the successful binding of CD into the scaffolds.

To further prove the electrostatic binding, the CS/nHA/CD scaffolds were immersed into gradient concentrations (0, 0.1, 0.5, 1, 2 M) of NaCl solution. As shown in Figure S3, there was almost no CD absorption found in the pure water and 0.1 M NaCl solution during 24 h, illustrating negligible impact on the integrity of the scaffolds. When the ionic strength increased to the range of 0.5–2 M, some CD released into the solution from the scaffolds. Moreover, the release amount of CD was closely correlated with the ionic strength and immersing time.

The temperature changes of various CS/nHA/CD and CS/nHA scaffolds under 808 nm NIR laser (1 W/cm^2) were carefully investigated. Taking advantage of the excellent photothermal effects of CD (Figure S4, Supporting Information), the CS/nHA/CD scaffolds possessed satisfactory photothermal performance. The photothermal effect was concentration and time dependent. As shown in Figure 2a–b and Figure S5a–b (Supporting Information), the temperatures of the CS/nHA/CD scaffolds (made with 3, 2, 1 mg/mL CD) in a wet state reached up to 68.4, 65.6, and 62.8 °C, respectively, whereas the temperature of the pure CS/nHA scaffold only rose to 31.4 °C after 10 min of irradiation (808 nm, 1 W/cm^2). The photothermal effect was also measured, while the scaffolds were soaking in PBS solution. As shown in Figure 2c and Figure S5c, the temperature of the solution around the CS/nHA/CD scaffolds (made with 3, 2, 1 mg/mL CD) reached 52.6, 47.5, and 41.8 °C, respectively, whereas it was only 30.7 °C around the pure CS/nHA scaffold after 10 min of NIR irradiation (808 nm, 1 W/cm^2).

Hyperthermia over 50 °C can damage DNA and cause irreversible protein denaturation in tumor cells.[28] After considering the potential application *in vivo* including tumor and infection treatment, 3 mg/mL was chosen as the best concentration of CD for producing CS/nHA/CD scaffolds in this study because of their appropriate photothermal performance. We further performed the *in vivo* photothermal study by implanting the CS/nHA/CD and CS/nHA scaffolds into the tumor-bearing mice. Then the tumor site was treated with 10 min of NIR (1 W/cm^2) irradiation, and the temperature change was captured by the IR camera. As shown in Figure 2de, the temperature of the tumor center could reach 51.4 °C in the CS/nHA/CD+NIR group even when the scaffolds were implanted under the tumor. However, the center temperature was only 36.1 °C in the treatment of pure CS/nHA with NIR.

Biocompatibility and Cell Adhesion.

We tested the cytotoxicity of the scaffolds toward rBMSCs, and the results are shown in Figure S6 (Supporting Information). The optical densities (OD) values of the CS/nHA/CD scaffolds were similar to the CS/nHA scaffolds, and the OD values increased with culture time, showing good cell proliferation in all scaffolds. The hemolytic results (Figure S7, Supporting Information) showed that the supernatants of the prepared scaffolds and PBS were transparent, whereas a red color (the presence of released hemoglobin) was produced in DI water, suggesting that the scaffolds were nearly nonhemolytic to human red blood cells.

Interestingly, we found the morphologies of cell adhesion were different in the scaffolds. As presented in Figure 3a, rBMSCs in the CS/nHA/CD scaffolds showed a typical spindle-shape and discrete filopodia anchored stably on the surface of scaffold, whereas sphere-like

rBMSCs with unclear filopodia were found in the CS/nHA scaffolds. According to a previous study,[29] human mesenchymal stem cells (hMSCs) and human osteoblasts respectively showed spindle-shape and fibroblast-like morphology when grown on graphene substrates, whereas polygonal-shape and round-shaped cells were observed on SiO_2 substrates, respectively. Kilian et al.[30] have reported that hMSCs were stretched on the aligned SWNT networks and their high skeletal tension triggered mechanotransduction pathways, including adhesion mediated signaling or noncanonical Wnt signaling. We examined the adhesion- and cytoskeleton-related gene expression of rBMSCs in the scaffolds after 24 h of culture to further investigate the mechanism of enhanced cell adhesion in the CD doped scaffolds. Shown in Figure 3b, focal adhesion kinase (FAK) and vinculin (VCL) expression were significantly higher in the CS/nHA/CD scaffolds compared to the CS/nHA scaffolds ($p < 0.01$ and 0.05, respectively). Paxillin (PXN) expression was also higher in the CS/nHA/CD scaffolds than the CS/nHA scaffolds at the margin of statistical significance ($p = 0.054$). These results demonstrated that CD doped scaffolds promoted rBMSCs adhesion performance through the focal adhesion and actin cytoskeleton pathways.

Focal adhesion complexes are composed of transmembrane integrin receptors and intracellular proteins, including FAK, PXN, and VCL.[31] FAK can recruit other focal contact proteins or their regulators, promote changes in actin and microtubule structures, and regulate cell–cell contacts.[32] PXL interacts with FAK and/or VCL and is associated with cell adhesion, actin-based cytoskeletons, and cell growth.[33] VCL is also important in cell adhesion, morphology, and growth, interacting with actin, tensin, and PXL.[34] Up-regulation of these genes in focal signaling pathways results in focal adhesion formation, changes in actin cytoskeleton structures, and cell spreading.[35] In addition, a previous study confirmed that rBMSCs adhered in a flattened, spread out shape benefit osteogenesis.[36]

In Vitro Osteogenesis and *in vivo* Osteoinductivity.

The good biocompatibility and enhanced cell adhesion effect of CS/nHA/CD scaffolds encouraged us to evaluate their osteogenic property. Figure 3c and 3d show the mRNA expression level of osteogenesis-related genes of rBMSCs in the scaffolds after 7 and 14 days of culture, respectively. On day 7, the expression level of alkaline phosphatase (ALP) genes was significantly higher in the CS/nHA/CD scaffolds compared to the CS/nHA scaffolds ($p < 0.05$). Early stage ALP activity is a key marker of the osteogenic differentiation,[37] suggesting that rBMSCs in the CS/nHA/CD scaffolds started differentiating into osteoblasts earlier than those in the pure CS/nHA scaffolds. On day 14, the expression of type I collagen (COL-I) and osteocalcin (OCN) was significantly higher in the pure CS/nHA/CD scaffolds compared to the CS/nHA scaffolds ($p < 0.01$ and 0.05, respectively). The up-regulated expression of these late-stage osteoblast differentiation- and bone matrix mineralization-related genes suggested the addition of CD enhanced bone matrix formation.

We further study the osteoinductivity of CS/nHA/CD scaffolds *in vivo* by using a classic rat model for porous scaffolds.[38] Figure 3e presents the three-dimensional reconstructed Micro-CT images of new bone formation in the scaffolds. Obviously, there was more new bone formation in the CS/nHA/CD scaffolds at 4 weeks after implantation compared to the

CS/nHA scaffolds. Furthermore, bone mineral density (BMD) analysis found that the average BMD was 205.55 and 183.9 mg/cm^3 in the CS/nHA/CD and CS/nHA scaffolds, respectively. BMD was significantly higher ($p < 0.05$) in the CS/nHA/CD scaffolds after 4 weeks of implantation (Figure 3f).

Correspondingly, histology study also confirmed better bone formation in the CS/nHA/CD scaffolds. Figure 4a shows the H&E staining of the scaffolds after 4 weeks of implantation. No lobulated neutrophils were found, and more osteocytes (green arrows) were observed in CS/nHA/CD scaffold scaffolds, suggesting that the scaffolds had good tissue compatibility and osteoinductivity. Moreover, collagen formation and vascularization in the scaffolds were stained with Masson's trichrome staining. As Figure 4b shows, collagen (stained in blue, yellow arrows) appeared and small blood vessels (red arrows) formed in both scaffolds. It is noteworthy that there was more collagen and vessel formation in the CS/nHA/CD scaffolds compared to the CS/nHA scaffolds.

Bone repair materials using carbon-based nanomaterials, such as carbon nanotubes and graphene/GO, are proven to induce stem cell differentiation into an osteogenic lineage.[17,39] Pan et al.[40] have fabricated multiwall MWNT/polycaprolac-tone scaffolds. The adding of MWNT into the scaffolds can enhanced the ALP level of rBMSCs. Another study by Ruan et al.[41] has found that the GO/carboxymethyl chitosan (CMC) scaffolds can up-regulate the osteogenesis-related genes and repair rat calvarial defects after implantation. The mechanism behind CD induced osteogensis is still unclear. Shao et al.[24] have reported citric acid-based CD and their derivative could promote osteogenic gene expression and enhance matrix mineralization. Moreover, CD exhibited better osteogenic performance through the mitogen-activated protein kinase (MAPK) pathway. CD are likely to increase ROS generation and then activate the expression of MAPK family members, including c-Jun-N-terminal kinases (JNKs), protein kinase 38 (p38), and runt-related transcription factor 2 (RUNX2) to promote the osteogenic differentiation of rBMSCs.

In Vitro and *in vivo* PTT for Osteosarcoma.

Bone tumors are one of the most prevalent tumors with the lowest long-term survival rate, representing a serious threat to human health and life.[42] Moreover, bone destruction and local recurrence following primary tumor surgery are common complications in bone tumor therapy.[43] In recent years, PTT, which is based on localized heating and utilizes photothermal conversion agents to absorb near-infrared (NIR, 700–1300 nm) light, has attracted increasing attention in cancer therapy applications.[28,44–47] This concept was lately introduced for three-dimensional scaffolds, but until recently, very few scaffolds have been fabricated with compositions or surface modifications using PTT agents to obtain photothermal effects.[48–52] These reports suggest that photothermal scaffolds can be ideal biomaterials for bone tumor therapy and tumor-induced bone defect repair.

CS/nHA/CD scaffolds were treated with NIR irradiation to detect the effectiveness of PTT toward osteosarcoma cells and tumor tissues. As shown in Figure 5a, cell viability was significantly lower in the CS/nHA/CD scaffolds under 1 W/cm^2 NIR irradiation compared to the other treatment groups. Live/dead staining (Figure 5b) further confirmed that almost all cells were dead (red) and that the remaining live cells (green) were vaguely observed in the

CS/nHA/CD+NIR group. In contrast, there were negligible dead cells (red) among the CS/nHA/CD, CS/nHA+NIR, and CS/nHA groups, which was consistent with the CCK-8 results. The morphology of UMR-106 cells in the CS/nHA/CD and CS/nHA scaffolds with or without NIR irradiation are shown in Figure 6c. The tumor cells in the CS/nHA/CD scaffolds showed typical characteristics of necrotic cells,[53] such as swollen and severe cell membrane damage, whereas the tumor cells had normal shapes in the other groups. These results illustrated outstanding tumor ablation *in vitro* by the CS/nHA/CD scaffolds in combination with PTT.

To date, there are no suitable models to evaluate bone tumor therapeutic effect and osteoinductivity at the same time.[48] Bone tumors can hardly establish in large animal models due to the immunological rejection. On the other hand, the bone size in the most used tumor models (e.g., nude mice) is too small. Moreover, surgical damage to highly malignant osteosarcoma may result in extensive bleeding and tumor systemic metastasis. Therefore, the *in vivo* PPT was studied by implanting the scaffold under the tumor in osteosarcoma-bearing mice. Figure 6a–b presents the visual images of tumors in different groups after 14 days of treatment. In the CS/nHA/CD, CS/nHA+NIR, and CS/nHA groups, the tumors were huge due to the highly malignant nature of osteosarcoma, whereas there were only small scars on the back of the mice and the tumors were effectively suppressed in the CS/nHA/CD+NIR group. A more detailed dynamic tumor volume was evaluated in Figure 6c. The tumors grew rapidly in the CS/nHA/CD, CS/nHA+NIR, and CS/nHA groups, but they were completely suppressed over time in the CS/nHA/CD+NIR group.

The histology changes in the scaffolds and tumors were also studied by H&E staining (Figure 7a). In the CS/nHA/CD, CS/nHA+NIR, and CS/nHA groups, tumor cells showed the typical pathological characteristics of osteosarcoma and had already invaded the scaffolds. However, severe damage at the tumor site can be found around the scaffold of the CS/nHA/CD+NIR group, such as the disappearance of cell nuclei, ambiguous intercellular gaps, and vague tumor structures. Moreover, tumor cell proliferation *in vivo* was measured by K_i-67 immunohistochemistry (IHC) staining (Figure 7b). It can be easily seen that the cells around the scaffolds in the CS/nHA/CD, CS/nHA+NIR, and CS/nHA groups overexpressed K_i-67 (dark brown color), indicating the fast growth of the osteosarcoma. For the CS/nHA/CD+NIR group, K_i-67 expression was negative (blue) in the tissue around the scaffold, suggesting the proliferation of osteosarcoma was effectively inhibited.

The *in vivo* safety of the CS/nHA/CD scaffolds was studied by H&E staining of the main organs in mice. As shown in Figure S8 (Supporting Information), main organs including heart, liver, spleen, lung, and kidney showed no damage or inflammation. All these results suggest that PTT with the CS/nHA/CD scaffold has advantages over traditional therapy, where NIR can exhibit strong penetrative ability in deep tissue, and that the scaffold can precisely ablate tumor tissue without damaging normal tissues by acting as a localized photothermal agent.

However, owing to the limited bone tumor model, the efficacy of photothermal scaffolds was currently investigated in a subcutaneous osteosarcoma rather than in bone.[48,50,52] For example, previously, Letfullin et al.[54] have simulated the photothermal behavior of gold

nanoparticles in biological hard tissue and found that it can be controlled by characteristics of the nanoparticles as well as laser wavelength and intensity. In regard to hard tissue irradiation, different approaches including placing optical fiber within hollow metal needle and sharpening silica fiber to create microneedles were made.[55,56] NIR based photothermal scaffolds were shown to be as effective in hard tissues as in soft tissues but remain to be further studied in a better model (e.g., orthotopic model).

In Vitro and *in vivo* Antibacterial Properties.

Bone infection and the related bone defects are other pressing problems in clinic. Current treatments include the removal of necrotic bone, administration of antibiotics, and reconstruction of the bone defects. However, these treatments are time-consuming, and their outcomes are unsatisfied. Therefore, bone scaffolds, which can kill clinical bacteria and fill the defect to promote bone formation at the same time, are desired to treat these defects. CS is a natural antibiotic, killing bacteria by preventing DNA replication or blocking transport of nutrient substance.[11,57] Thanks to the presence of CS, all scaffolds showed good antibacterial properties toward clinical bacteria *in vitro* (Figure S9, Supporting Information). Furthermore, PTT is also useful in the treatment of infection. Teng et al. reported that gold nanocrosses can efficiently eradicate bacteria by localized photothermal effect under NIR irradiation.[58] In the present study, the results regarding the antibacterial properties of the scaffolds with or without NIR are depicted in Figure 8a. The CS/nHA/CD+NIR group had significantly higher antibacterial activity toward pathogenic *S. aureus* and *E. coli* (with an antibacterial rate of 99% and 97%, respectively), whereas the antibacterial rates were approximately 75% in the other groups.

We further assessed the *in vivo* antibacterial effect by PTT using the CS/nHA/CD and CS/nHA scaffolds. As shown in Figure 8b. After 1 week of treatment, there was still a large number of *S. aureus* and *E. coli* colonies in the CS/nHA+NIR group, whereas the bacterial levels were significantly reduced in the CD/nHA/CD+NIR group. H&E staining of the samples (Figure 9a) showed many lobulated neutrophils (orange arrows) in the CS/nHA +NIR group due to inflammation and the injected bacteria. However, only minor inflammation occurred in the CS/nHA/CD+NIR group because of an enhanced antibacterial effect after NIR irradiation. Moreover, bacteria were observed in the CS/nHA+NIR groups by Giemsa staining (Figure 9b), but no obvious bacteria were found in the CS/nHA/CD +NIR groups, indicating that hyperthermia was also beneficial to the inhibition of bacterial growth. Therefore, CS/nHA/CD scaffolds with NIR irradiation exhibit enhanced antibacterial properties that can efficiently eliminate clinically relevant bacterial infections.

CONCLUSION

In this study, we successfully developed a novel CD doped CS/nHA (CS/nHA/CD) scaffold for bone regeneration and found that CD can promote osteogenesis within scaffolds. Notably, the CD doped scaffolds enhanced rBMSCs adhesion and osteogenic differentiation and promoted the formation of vascularized bone tissue. Moreover, simultaneous PTT based on a CS/nHA/CD scaffold under NIR laser can efficiently ablate tumors and guarantee the scaffold’s antibacterial properties in clinical infections. Hence, CS/nHA/CD scaffolds with

multifunctional characteristics can be used to repair bone defects and treat tumors and bacterial infections.

Supplementary Material

Refer to Web version on PubMed Central for supplementary material.

ACKNOWLEDGMENTS

We appreciate the financial support from the National Key Research and Development Program of China (2016YFB0700800, 2017YFB0702604), the National Natural Science Foundation of China (21620102004, 81402409), the Natural Science Foundation of Guangdong Province (2015A030312004), and the Science and Technology Planning Project of Guangzhou City (201604020110) as well as the National Institutes of Health R01MH103133 and R21GM126532 and the Human Frontier Science RGY-0090/2014.

REFERENCES

(1). Dimitriou R, Elena J, Dennis MG, and Giannoudis PV (2011) Bone Regeneration: Current Concepts and Future Directions. BMC Med. 9, 66–75. [PubMed: 21627784]

(2). Hutmacher DW (2000) Scaffolds in Tissue Engineering Bone and Cartilage. Biomaterials 21, 2529–2543. [PubMed: 11071603]

(3). Roseti L, Parisi V, Petretta M, Cavallo C, Desando G, Bartolotti I, and Grigolo B (2017) Scaffolds for Bone Tissue Engineering: State of the Art and New Perspectives. Mater. Sci. Eng., C 78, 1246–1262.

(4). Spoerke ED, Murray NG, Li H, Brinson LC, Dunand DC, and Stupp SI (2005) A Bioactive Titanium Foam Scaffold for Bone Repair. Acta Biomater. 1, 523–533. [PubMed: 16701832]

(5). Deng C, Yao Q, Feng C, Li J, Wang L, Cheng G, Shi M, Chen L, Chang J, and Wu C (2017) 3D Printing of Bilineage Constructive Biomaterials for Bone and Cartilage Regeneration. Adv. Funct. Mater 27, 1703117.

(6). Hu X, Wang Y, Tan Y, Jie W, Liu H, Wang Y, Shuang Y, Shi M, Zhao S, Zhang Y, et al. (2017) A Difunctional Regeneration Scaffold for Knee Repair Based on Aptamer-Directed Cell Recruitment. Adv. Mater 29, 1605235.

(7). Ghosh B, and Urban MW (2009) Self-Repairing Oxetane-Substituted Chitosan Polyurethane Networks. Science 323, 1458–1460. [PubMed: 19286550]

(8). Li L, Li M, Li D, He P, Xia H, Zhang Y, and Mao C (2014) Chemical Functionalization of Bone Implants with Nano-particle-Stabilized Chitosan and Methotrexate for Inhibiting Both Osteoclastoma Formation and Bacterial Infection. J. Mater. Chem. B 2, 5952–5961. [PubMed: 25177491]

(9). Sun TW, Yu WL, Zhu YJ, Yang RL, Shen YQ, Chen DY, He YH, and Chen F (2017) Hydroxyapatite Nanowire@Magnesium Silicate Core–Shell Hierarchical Nanocomposite: Synthesis and Application in Bone Regeneration. ACS Appl. Mater. Interfaces 9, 16435–16447. [PubMed: 28481082]

(10). Lee SB, Kwon JS, Lee YK, Kim KM, and Kim KN (2012) Bioactivity and Mechanical Properties of Collagen Composite Membranes Reinforced by Chitosan and β-Tricalcium Phosphate. J. Biomed. Mater. Res., Part B 100B, 1935–1942.

(11). Cheung RCF, Ng TB, Wong JH, and Chan WY (2015) Chitosan: An Update on Potential Biomedical and Pharmaceutical Applications. Mar. Drugs 13, 5156–5186. [PubMed: 26287217]

(12). Lu Y, Li M, Li L, Wei S, Hu X, Wang X, Shan G, Zhang Y, Xia H, and Yin Q (2018) High-Activity Chitosan/Nano Hydroxyapatite/Zoledronic Acid Scaffolds for Simultaneous Tumor Inhibition, Bone Repair and Infection Eradication. Mater. Sci. Eng., C 82, 225–233.

(13). Lu Y, Li L, Zhu Y, Wang X, Li M, Li Z, Hu X, Zhang Y, Yin Q, Xia H, et al. (2018) Multifunctional Copper-Containing Carboxymethyl Chitosan/Alginate Scaffolds for Eradicating Clinical Bacterial Infection and Promoting Bone Formation. ACS Appl. Mater. Interfaces 10, 127–138. [PubMed: 29256580]

(14). Shen X, Zhang Y, Gu Y, Xu Y, Liu Y, Li B, and Chen L (2016) Sequential and Sustained Release of SDF-1 and BMP-2 from Silk Fibroin-Nanohydroxyapatite Scaffold for the Enhancement of Bone Regeneration. Biomaterials 106, 205–216. [PubMed: 27566869]

(15). Li L, Zhou G, Wang Y, Yang G, Ding S, and Zhou S (2015) Controlled Dual Delivery of BMP-2 and Dexamethasone by Nanoparticle-Embedded Electrospun Nanofibers for the Efficient Repair of Critical-Sized Rat Calvarial Defect. Biomaterials 37, 218–229. [PubMed: 25453952]

(16). Kempen DHR, Lu L, Heijink A, Hefferan TE, Creemers LB, Maran A, Yaszemski MJ, and Dhert WJA (2009) Effect of Local Sequential VEGF and BMP-2 Delivery on Ectopic and Orthotopic Bone Regeneration. Biomaterials 30, 2816–2825. [PubMed: 19232714]

(17). Kang ES, Kim DS, Suhito IR, Choo SS, Kim SJ, Song I, and Kim TH (2017) Guiding Osteogenesis of Mesenchymal Stem Cells Using Carbon-Based Nanomaterials. Nano Convergence 4, 2–15. [PubMed: 28191446]

(18). Ku SH, Lee M, and Park CB (2013) Carbon-Based Nanomaterials for Tissue Engineering. Adv. Healthcare Mater 2, 244–260.

(19). Qu S, Wang X, Lu Q, Liu X, and Wang L (2012) A Biocompatible Fluorescent Ink Based on Water-Soluble Luminescent Carbon Nanodots. Angew. Chem., Int. Ed 51, 12215–12218.

(20). Xu M, He G, Li Z, He F, Gao F, Su Y, Zhang L, Yang Z, and Zhang Y (2014) A Green Heterogeneous Synthesis of N-Doped Carbon Dots and Their Photoluminescence Applications in Solid and Aqueous States. Nanoscale 6, 10307–10315. [PubMed: 25069763]

(21). Liu X, Jiang H, Ye J, Zhao C, Gao S, Wu C, Li C, Li J, and Wang X (2016) Nitrogen-Doped Carbon Quantum Dot Stabilized Magnetic Iron Oxide Nanoprobe for Fluorescence, Magnetic Resonance, and Computed Tomography Triple-Modal *in vivo* Bioimaging. Adv. Funct. Mater 26, 8694–8706.

(22). Huang P, Lin J, Wang X, Wang Z, Zhang C, He M, Wang K, Chen F, Li Z, Shen G, et al. (2012) Light-Triggered Theranostics Based on Photosensitizer-Conjugated Carbon Dots for Simultaneous Enhanced-Fluorescence Imaging and Photodynamic Therapy. Adv. Mater 24, 5104–5110. [PubMed: 22718562]

(23). Peng Z, Miyanji EH, Zhou Y, Pardo J, Hettiarachchi SD, Li S, Blackwelder PL, Skromne I, and Leblanc RM (2017) Carbon Dots: Promising Biomaterials for Bone-Specific Imaging and Drug Delivery. Nanoscale 9, 17533–17543. [PubMed: 29110000]

(24). Shao D, Lu M, Xu D, Zheng X, Pan Y, Song Y, Xu J, Li M, Zhang M, Li J, et al. (2017) Carbon Dots for Tracking and Promoting the Osteogenic Differentiation of Mesenchymal Stem Cells. Biomater. Sci 5, 1820–1827. [PubMed: 28657615]

(25). Erdal N, and Hakkarainen M (2018) Construction of Bioactive and Reinforced Bioresorbable Nanocomposites by Reduced Nano-Graphene Oxide Carbon Dots. Biomacromolecules 19, 1074–1081. [PubMed: 29438617]

(26). Khajuria DK, Kumar VB, Gigi D, Gedanken A, and Karasik D (2018) Accelerated Bone Regeneration by Nitrogen-doped Carbon Dots Functionalized with Hydroxyapatite Nano-particles. ACS Appl. Mater. Interfaces 10, 19373–19385. [PubMed: 29782148]

(27). Ge J, Jia Q, Liu W, Guo L, Liu Q, Lan M, Zhang H, Meng X, and Wang P (2015) Red-Emissive Carbon Dots for Fluorescent, Photoacoustic, and Thermal Theranostics in Living Mice. Adv. Mater 27, 4169–4177. [PubMed: 26045099]

(28). Jaque D, Martínez ML, Del RB, Harogonzalez P, Benayas A, Plaza JL, Martín RE, and García SJ (2014) Nanoparticles for Photothermal Therapies. Nanoscale 6, 9494–9530. [PubMed: 25030381]

(29). Kalbacova M, Broz A, Kong J, and Kalbac M (2010) Graphene Substrates Promote Adherence of Human Osteoblasts and Mesenchymal Stromal Cells. Carbon 48, 4323–4329.

(30). Kilian KA, Bugarija B, Lahn BT, and Mrksich M (2010) Geometric Cues for Directing the Differentiation of Mesenchymal Stem Cells. Proc. Natl. Acad. Sci. U. S. A 107, 4872–4877. [PubMed: 20194780]

(31). Lo SH (2006) Focal Adhesions: What's New Inside. Dev. Biol 294, 280–291. [PubMed: 16650401]

(32). Mitra SK, Hanson DA, and Schlaepfer DD (2005) Focal Adhesion Kinase: In Command and Control of Cell Motility. Nat. Rev. Mol. Cell Biol 6, 56–68. [PubMed: 15688067]

(33). Brown MC, Perrotta JA, and Turner CE (1996) Identification of LIM3 as the Principal Determinant of Paxillin Focal Adhesion Localization and Characterization of A Novel Motif on Paxillin Directing Vinculin and Focal Adhesion Kinase Binding. J. Cell Biol 135, 1109–1123. [PubMed: 8922390]

(34). Hemmings L, Barry ST, and Critchley DR (1995) Cell-Matrix Adhesion: Structure and Regulation. Biochem. Soc. Trans 23, 619–626. [PubMed: 8566429]

(35). Carragher NO, and Frame MC (2004) Focal Adhesion and Actin Dynamics: A Place where Kinases and Proteases Meet to Promote Invasion. Trends Cell Biol. 14, 241–249. [PubMed: 15130580]

(36). Mcbeath R, Pirone DM, Nelson CM, Bhadriraju K, Chen CS (2004) Cell Shape, Cytoskeletal Tension, and RhoA Regulate Stem Cell Lineage Commitment. Dev. Cell 6, 483–495. [PubMed: 15068789]

(37). Li M, He P, Wu Y, Zhang Y, Xia H, Zheng Y, and Han Y (2016) Stimulatory Effects of the Degradation Products from Ca-Sr Alloy on the Osteogenesis through Regulating ERK Signaling Pathway. Sci. Rep 6, 32323.

(38). Li Z, Ramay HR, Huach KD, Xiao D, and Zhang, (2005) Chitosan-Alginate Hybrid Scaffolds for Bone Tissue Engineering. Biomaterials 26, 3919–3928. [PubMed: 15626439]

(39). Cha C, Su RS, Annabi N, Dokmeci MR, Khademhosseini A (2013) Carbon-Based Nanomaterials: Multi-Functional Materials for Biomedical Engineering. ACS Nano 7, 2891–2897. [PubMed: 23560817]

(40). Pan L, Pei X, He R, Wan Q, and Wang J (2012) Multiwall Carbon Nanotubes/Polycaprolactone Composites for Bone Tissue Engineering Application. Colloids Surf., B 93, 226–234.

(41). Ruan J, Wang X, Yu Z, Wang Z, Xie Q, Zhang D, Huang Y, Zhou H, Bi X, and Xiao C (2016) Enhanced Physiochemical and Mechanical Performance of Chitosan-Grafted Graphene Oxide for Superior Osteoinductivity. Adv. Funct. Mater 26, 1085–1097.

(42). Ward E, Desantis C, Robbins A, Kohler B, and Jemal, (2014) Childhood and Adolescent Cancer Statistics, 2014. Ca-Cancer J. Clin 64, 83–103. [PubMed: 24488779]

(43). Grimer RJ (2005) Surgical Options for Children Osteosarcoma. Lancet Oncol. 6, 85–92. [PubMed: 15683817]

(44). Li L, Rashidi LH, Yao M, Ma L, Chen L, Zhang, Zhang Y, and Chen W (2017) CuS Nanoagents for Photodynamic and Photothermal Therapies: Phenomena and Possible Mechanisms. Photodiagn. Photodyn. Ther 19, 5–14.

(45). Li L, Yang X, Hu X, Lu Y, Wang L, Peng M, Xia H, Q., Zhang Y, and Han G (2017) Multifunctional Cu39S28 Hollow Nanopeanuts for *in vivo* Targeted Photothermal Chemotherapy. Mater. Chem. B 5, 6740–6751.

(46). Li L, Lu Y, Jiang C, Zhu Y, Yang X, Hu X, Lin Z, Zhang Y, Peng M, Xia H, et al. (2018) Actively Targeted Deep Tissue Imaging and Photothermal-Chemo Therapy of Breast Cancer Antibody-Functionalized Drug-Loaded X-Ray-Responsive Bismuth Sulfide@Mesoporous Silica Core–Shell Nanoparticles. Adv. Funct. Mater 28, 1704623.

(47). Wang Li., Long NJ, Li L, Lu Y, Li M, Cao J, Zhang, Zhang Q, Xu S, Yang Z, et al. (2018) Multi-Functional Bismuth-Doped Bioglasses: Combining Bioactivity and Photothermal Response for Bone Tumor Treatment and Tissue Repair. Light: sci. Appl 7, 1.

(48). Ma H, Jiang C, Zhai D, Luo Y, Chen Y, Lv F, Yi, Deng Y, Wang J, Chang J, et al. (2016) A Bifunctional Biomaterial with Photothermal Effect for Tumor Therapy and Bone Regeneration. Adv. Funct. Mater 26, 1197–1208.

(49). Zhang J, Li J, Chen S, Kawazoe N, and Chen G (2016) Preparation of Gelatin/Fe3O4 Composite Scaffolds for Enhanced Repeatable Cancer Cell Ablation. J. Mater. Chem. B 4, 5664–5672.

(50). Ma H, Luo J, Sun Z, Xia L, Shi M, Liu M, Chang J, Wu C (2016) 3D Printing of Biomaterials with Mussel-Inspired Nanostructures for Tumor Therapy and Tissue Regeneration. Biomaterials 111, 138–148. [PubMed: 27728813]

(51). Zhang J, Li J, Kawazoe N, and Chen G (2017) Composite Scaffolds of Gelatin and Gold Nanoparticles with Tunable Size Shape for Photothermal Cancer Therapy. J. Mater. Chem. B 5, 245–253.

(52). Yang B, Yin J, Chen Y, Pan S, Yao H, Gao Y, and Shi, (2018) 2D-Black-Phosphorus-Reinforced 3D-Printed Scaffolds:A Stepwise Countermeasure for Osteosarcoma. Adv. Mater 30, 1705611.

(53). Majno G, and Joris I (1995) An Overview of Cell Death. Am. J. Pathol 146, 3–15. [PubMed: 7856735]

(54). Letfullin RR, Rice CE, and George TF (2011) Theoretical Study of Bone Cancer Therapy by Plasmonic Nanoparticles. Ther. Delivery 2, 1259–1273.

(55). Kang D, and Jung B (2010) Treatment Feasibility Study of Osteoporosis Using Minimal Invasive Laser Needle System. Proc. SPIE 7548, 75484C.

(56). Kosoglu MA, Hood RL, Chen Y, Xu Y, Rylander MN, and Rylander CG (2010) Fiber Optic Microneedles for Transdermal Light Delivery: Ex Vivo Porcine Skin Penetration Experiments. J. Biomech. Eng 132, 091014.

(57). Zheng LY, and Zhu JF (2003) Study on Antimicrobial Activity of Chitosan with Different Molecular Weights. Carbohydr. Polym 54, 527–530.

(58). Teng CP, Zhou T, Ye E, Liu S, Koh LD, Low M, Loh XJ, Win KY, Zhang L, and Han MY (2016) Effective Targeted Photothermal Ablation of Multidrug Resistant Bacteria and Their Biofilms with NIR-Absorbing Gold Nanocrosses. Adv. Healthcare Mater 5, 2122–2130.

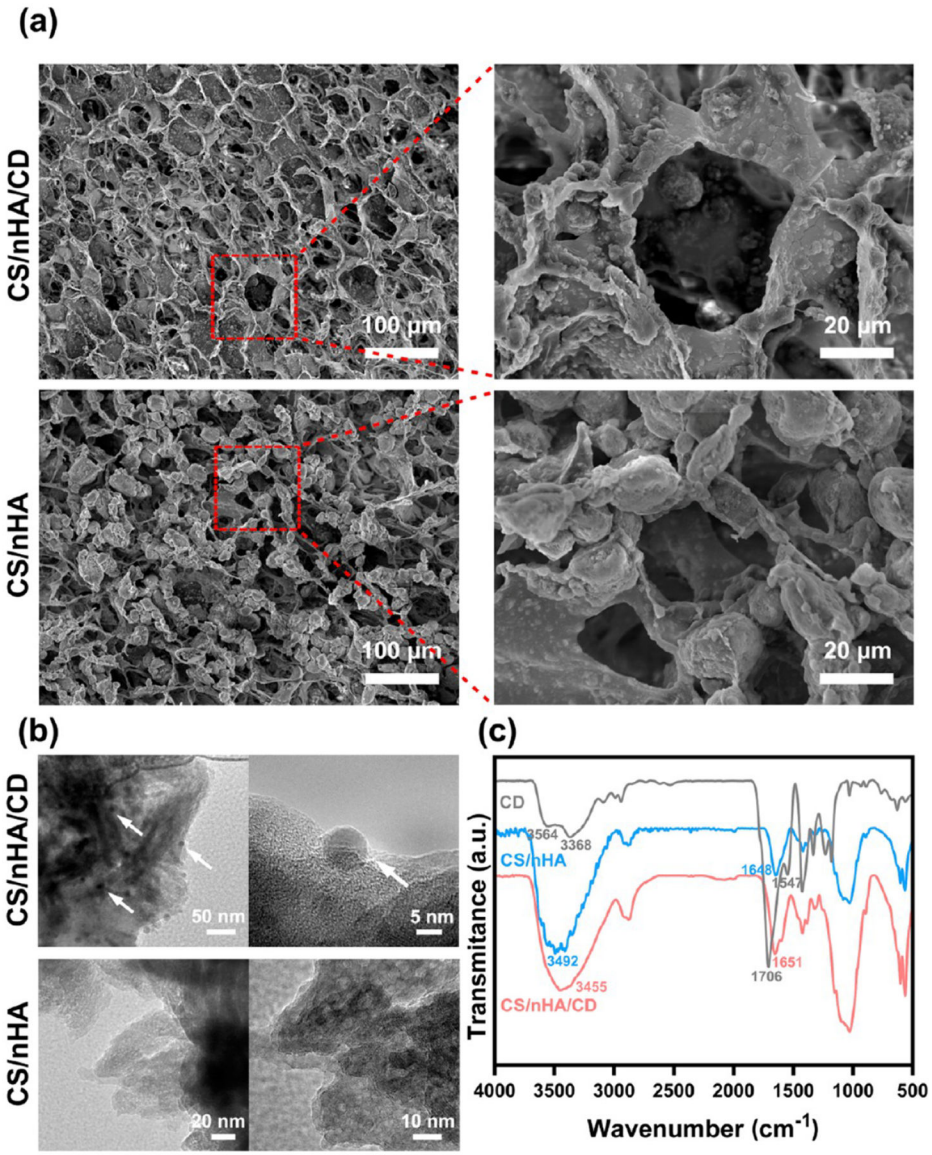

Figure 1.

Characterization of the scaffolds. (a) SEM analysis of the CS/nHA/CD and the CS/nHA scaffolds. (b) TEM analysis of the CS/nHA/CD and the CS/nHA scaffolds. The white arrows show the CD in the CS/nHA/CD scaffolds. (c) FTIR spectra of the scaffolds.

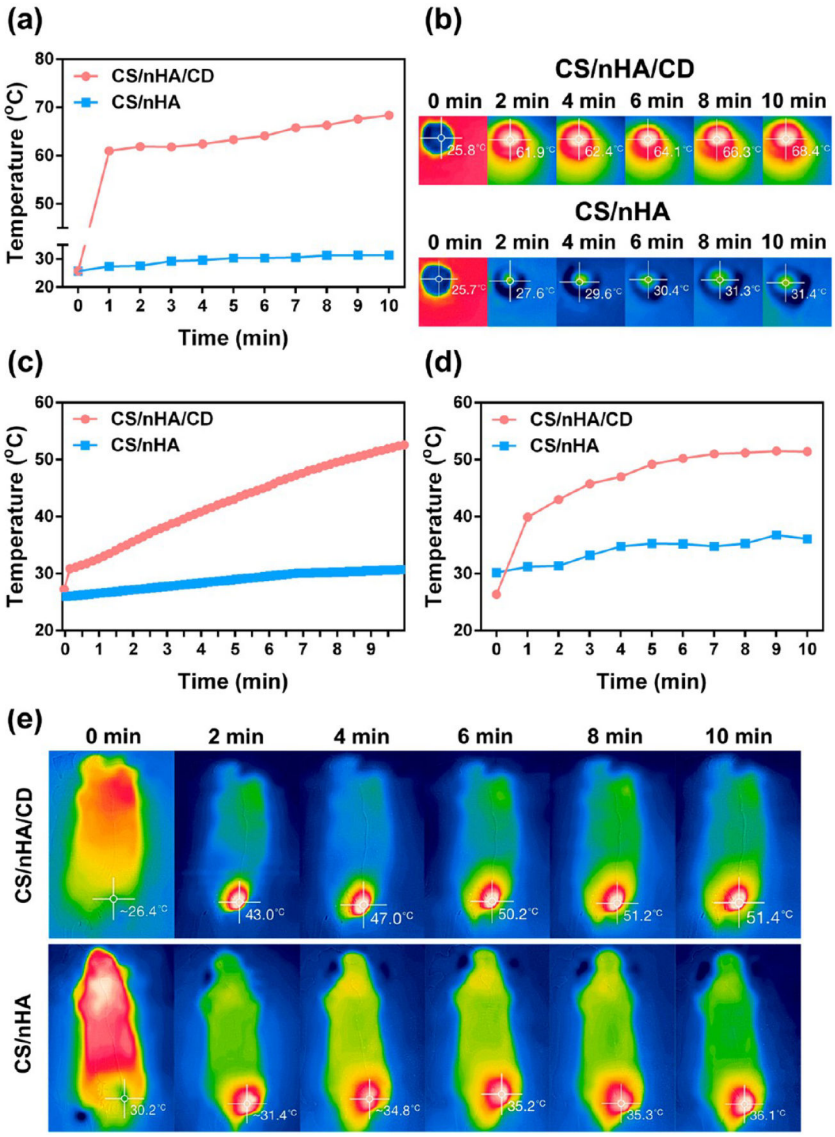

Figure 2.

In vitro and *in vivo* photothermal effect of the scaffolds. (a) Quantitative temperature changes of the CS/nHA/CD and the CS/nHA scaffolds in a wet state under 1 W/cm^2, 808 nm laser irradiation for 10 min derived from the IR camera measurements shown in (b). (b) IR image of the scaffolds in a wet state captured every 2 min (from left to right) under 1 W/cm^2, 808 nm laser irradiation for 10 min. (c) Quantitative temperature changes of the PBS solution around the soaked scaffolds under 1 W/cm^2, 808 nm laser irradiation for 10 min. (d) Quantitative temperature changes of the mouse tumor sites under 1 W/cm^2, 808 nm laser irradiation for 10 min after implantation of the scaffolds derived from the IR camera measurements shown in (e). (e) IR images of the mice captured every 2 min (from left to right) showing the temperature change at tumor sites under 1 W/cm^2, 808 nm laser irradiation. The light was only applied to the tumors during the measurements, which were made after implantation of the CS/nHA/CD and CS/nHA scaffolds.

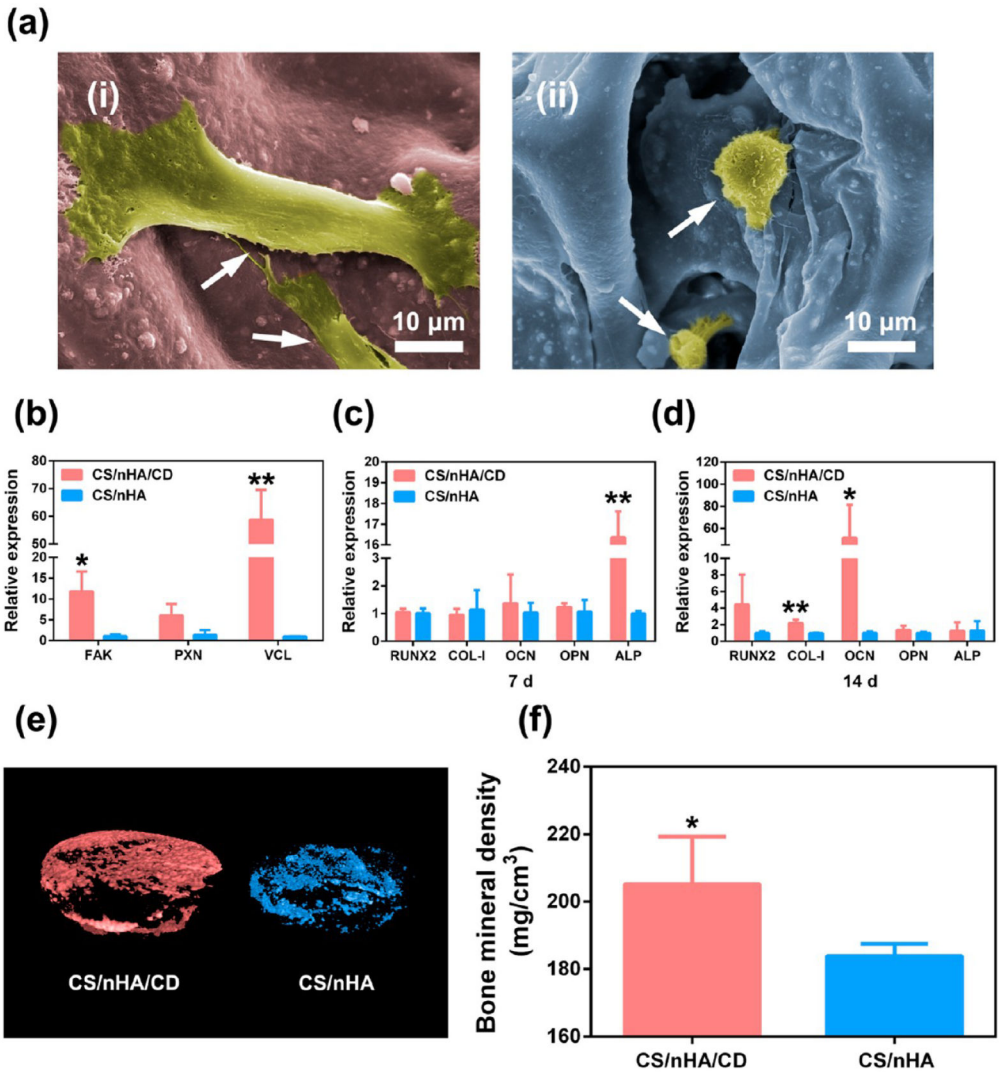

Figure 3.

Cell adhesion and osteogenesis. (a) Cell morphology within the scaffolds. (i), (ii) rBMSCs in the CS/nHA/CD and the CS/nHA scaffolds, respectively. rBMSCs (white arrows) exhibited more obvious spindle shapes and discrete filopodia in the CS/nHA/CD scaffolds than in the CS/nHA scaffolds. (b) The relative expression levels of genes related to cell adhesion in the scaffolds. Focal adhesion pathway genes expression of FAK and VCL was significantly higher in the CS/nHA/CD scaffolds. PXN expression was also higher in the CS/nHA/CD scaffolds. (c-d) Relative expression of osteogenesis-related genes after 7 and 14 days of culture, respectively. The expression level of ALP was significantly higher in the CS/nHA/CD scaffolds compared to the CS/nHA scaffolds on day 7, and the expression levels of COL-1 and OCN were significantly higher in the CS/nHA/CD scaffolds compared to the CS/nHA scaffolds on day 14. (e) Micro-CT 3D reconstruction models of the newly formed bone in the scaffolds. More new bone formation was found in CS/nHA/CD scaffolds at 4 weeks. (f) BMD of the new formed bone in the scaffolds. BMD was significantly higher in the CS/nHA/Cu scaffolds after 4 weeks of implantation. Each value is the mean ± standard deviation; *$p < 0.05$, **$p < 0.01$ compared to the CS/nHA scaffolds.

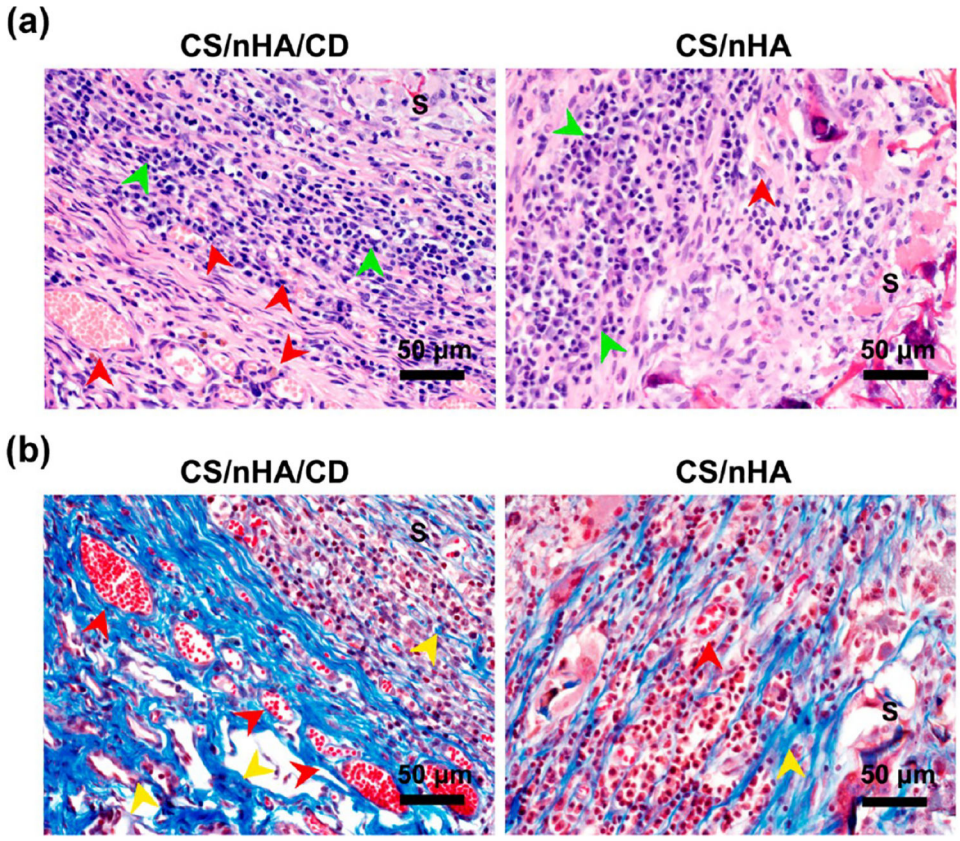

Figure 4.

Histological photographs of the harvested samples. (a) H&E staining showing that there were no lobulated neutrophils in any scaffolds, and there were more osteocytes (green arrows) in the CS/nHA/CD scaffolds than in the CS/nHA scaffolds. Many more vessels (red arrows) were found in the CS/nHA/CD scaffolds than in the CS/nHA scaffolds. (b) Masson's trichrome staining showed that more collagen (yellow arrows) and vessels (red arrows) were found in the CS/nHA/CD scaffolds than in the CS/nHA scaffolds. S represents the scaffolds.

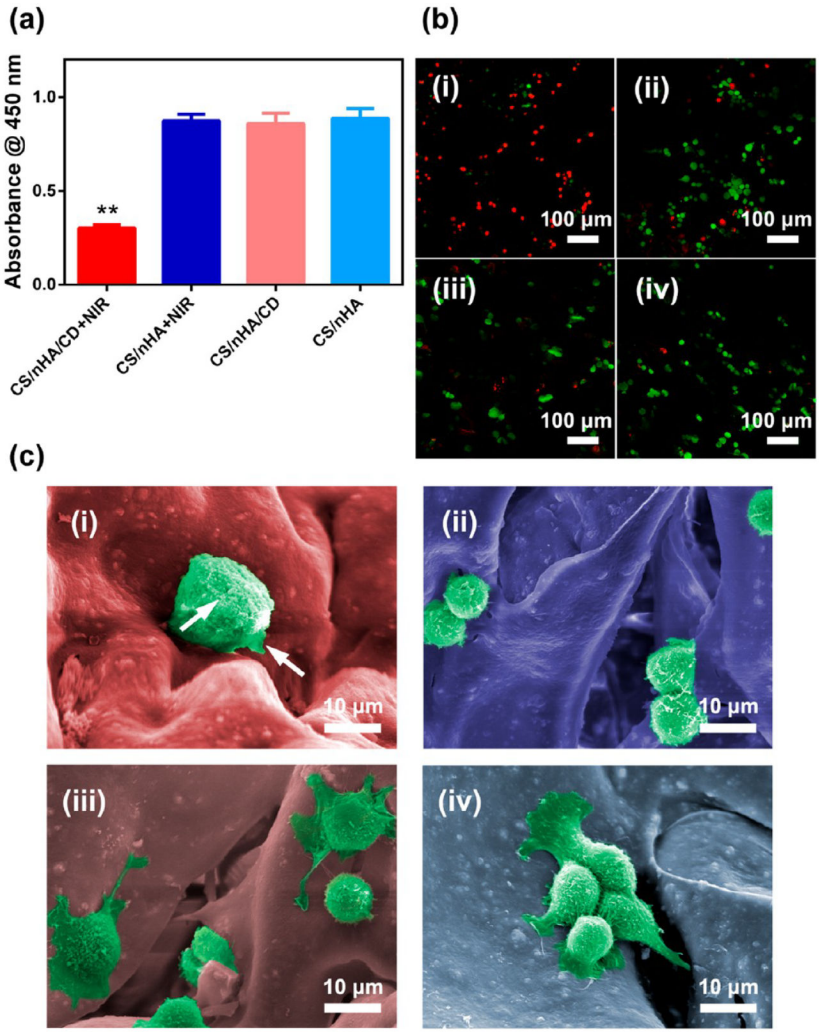

Figure 5.

In vitro PTT with the scaffolds. (a) Tumor cell killing effect of the CS/nHA/CD and CS/nHA scaffolds with or without 808 nm laser irradiation for 10 min. (b) Confocal laser scanning microscopy images of live/dead stained tumor cells with different treatments. (i-iv) CS/nHA/CD+NIR, CS/nHA+NIR, CS/nHA/CD, and CS/nHA, respectively. Most cells were dead (red) in the CS/nHA/CD+NIR group, indicating an excellent tumor ablation effect. (c) SEM images of the tumor cells with different treatments. (i-iv) CS/nHA/CD+NIR, CS/nHA +NIR, CS/nHA/CD, and CS/nHA, respectively. Tumor cells were swollen, and the cell membrane was damaged (highlighted by white arrows) in the CS/nHA/CD +NIR group, whereas they showed normal morphology in the other groups. Each value is the mean ± standard deviation; *$p < 0.05$, **$p < 0.01$.

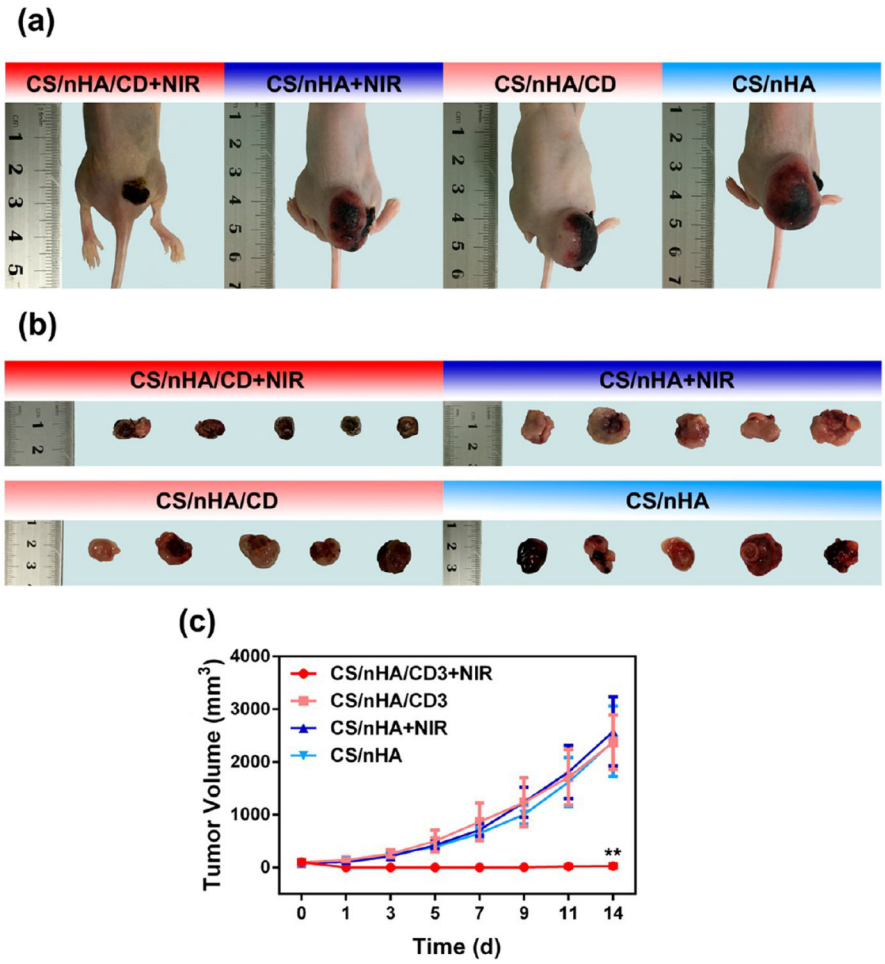

Figure 6.

in vivo PTT with the scaffolds. (a) Representative photos of tumor-bearing nude mice in different groups 14 days after treatment. In the CS/nHA/CD+NIR group, there was only a small scar on the back of the mouse, and the tumor had disappeared. (b) Tumors collected from different groups of mice 14 days after treatment. In the CS/nHA/CD+NIR group, tumors were totally suppressed. (c) Tumor volume growth curves of different treatment groups over a period of 14 days. The tumor volume of the CS/nHA/CD+NIR group was significantly lower than those of the other groups. *$p < 0.05$, **$p < 0.01$.

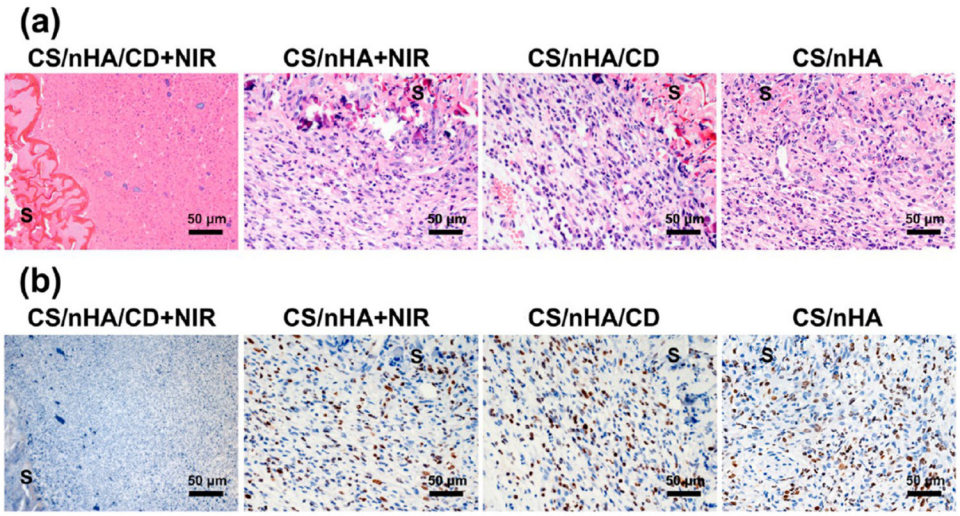

Figure 7.

Histological photographs of the scaffolds and tumors. (a) H&E staining of the scaffolds and tumors harvested from different mouse groups. Tumor cells were severely damaged in the CS/nHA/CD+NIR group. (b) K_i-67 IHC staining of the scaffolds and tumor tissues. K_i-67 was negatively expressed in the CS/nHA/CD+NIR group but was highly expressed in the other groups. S represents the scaffolds.

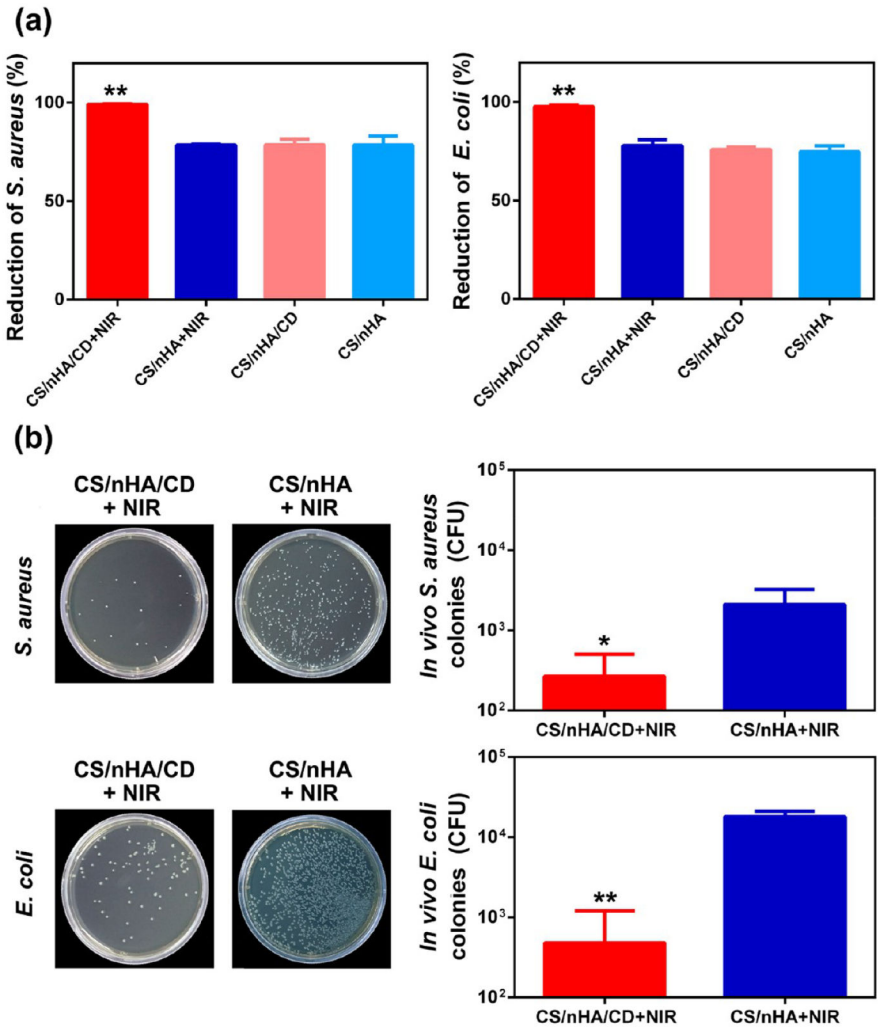

Figure 8.

Antibacterial properties of the scaffolds. (a) *In vitro* antibacterial rate against clinically relevant *S. aureus* (left) and *E. coli* (right) of the different groups. The CS/nHA/CD+NIR group showed significantly higher antibacterial activity against clinical bacteria. (b) Number of clinically relevant *S. aureus* (top) and *E. coli* (bottom) bacterial colonies after bacteria from the harvested samples was cultured for 24 h after 1 week treatments *in vivo*. Each value is the mean ± standard deviation; $*p < 0.05$, $**p < 0.01$.

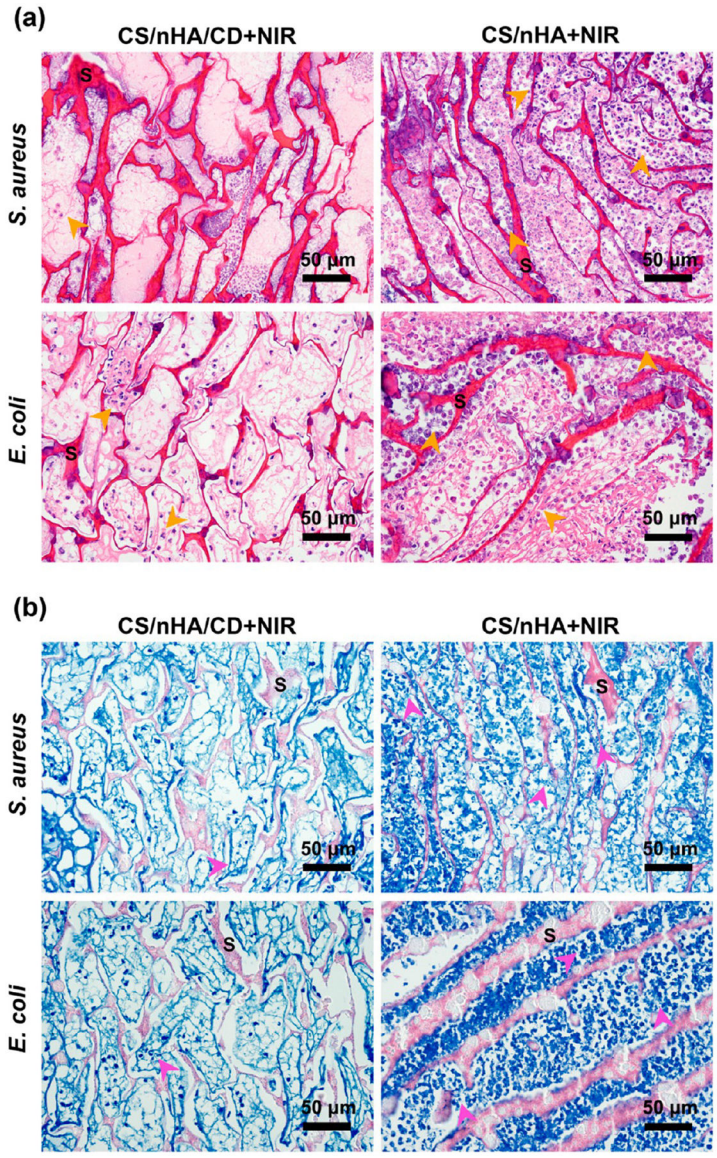

Figure 9.

Histological photographs of the scaffolds and bacteria. (a) H&E staining of the samples harvested from the different groups. A small amount of lobulated neutrophils (orange arrows) was found in the CS/nHA/CD+NIR group, whereas many lobulated neutrophils were seen in the CS/nHA+NIR group. (b) Giemsa staining of the samples. Very few bacteria (pink arrows) were found in the CS/nHA/CD+NIR group, but much more bacteria were observed in the CS/nHA+NIR group. S represents the scaffolds.